A Lyapunov-Based Nonlinear Power Control Algorithm for Grid-Connected VSCs

Fan, Bo; Wang, Xiongfei

Published in:
IEEE Transactions on Industrial Electronics

DOI (link to publication from Publisher):
10.1109/TIE.2021.3065614

Publication date:
2021

Document Version
Accepted author manuscript, peer reviewed version

A Lyapunov-Based Nonlinear Power Control Algorithm for Grid-Connected VSCs

Bo Fan, *Member, IEEE*, and Xiongfei Wang, *Senior Member, IEEE*

***Abstract*—For grid-connected voltage source converters (VSCs), it is commonly required that its power outputs can track the power references given by operators under various grid conditions. To achieve this objective, this article presents a Lyapunov-based nonlinear power control algorithm. The system dynamics is developed in the stationary frame, which facilitates the design of the control algorithm in the absence of phase-locked loops (PLLs) that may cause instability issues in ultra-weak grids. A virtual resistance is then introduced to allow fast power tracking performance and relax the requirement on accurate system parameters. Further, to simplify the control design, the quasi-stationary line (QSL) impedance model is applied, based on which a nonlinear control algorithm that only utilizes the output voltage and current information is developed. Afterward, the stability of the closed-loop system is analyzed via the Lyapunov theory. The theoretical results illustrate that the power regulation goal can be achieved and the VSC can maintain synchronization with the power grid. Finally, experimental results demonstrate the effectiveness of the proposed control algorithm under temporary grid faults and various short circuit ratios (SCRs).**

***Index Terms*—Nonlinear power regulation, grid-connected voltage source converter, Lyapunov theory, ultra-weak grid.**

I. Introduction

In the past decades, voltage source converters (VSCs) have been widely applied in power grids due to their flexibility in control and operation, e.g., microgrids [1], renewable energy systems [2], flexible ac transmission systems [3], etc. For a grid-connected VSC, a common control objective is to regulate its active and reactive power outputs to track their references [4], [5].

Traditionally, voltage-oriented vector-current control [6], [7] methods are utilized to achieve this objective. A phase-locked loop (PLL) is adopted to synchronize the VSC with the grid [8]. However, the PLL-based synchronization strategy may suffer from stability issues, especially when the VSC is connected to a weak grid [9], [10]. To address the instability issue induced by the PLLs, one solution is to introduce extra feedforward or feedback terms in the current control loop, such as the output impedance reshaping method [11] and small-signal disturbance compensation control [12]. However, these solutions increase the implementation complexity of the current control loop and are dependent on the operating point of the system. An alternative is to modify the PLL based on the concept of complex phase angle vectors to eliminate the frequency-coupling terms induced by traditional PLLs [13]. Recently, an improved parameter tuning method is presented in [14] to alleviate the negative impact of PLLs in weak grids. Although the instability effect of the PLL is mitigated by these strategies, it is still difficult to maintain the stability of VSCs connected to ultra-weak power grids [15]. Moreover, the nonlinearities of PLL dynamics, which are usually ignored in the aforementioned literature, may jeopardize the stability of these PLL-based controllers under large grid disturbances [16], [17].

Based on the aforementioned analysis, control algorithms without PLLs are preferred to ensure the stability of grid-connected VSCs. In [18], a PLL-free direct power control (DPC) strategy is developed based on the instantaneous active and reactive power theory. Further, a model predictive DPC strategy is proposed to optimize the switching frequency of the VSC [19]. However, since the switching frequency varies with the VSCs' power outputs when using these strategies, undesirable broadband harmonics may be injected into the power grid. Extra efforts on the filter design are therefore required to eliminate these harmonics. To deal with this problem, a DPC strategy using space-vector modulation is proposed with constant switching frequency [20]. Nevertheless, the stability analyses in weak grids are not performed in [20]. Recently, Gui *et. al.* [21] developed a voltage-modulated DPC method for weak grid-connected VSCs. Better control performance is achieved by eliminating nonlinear terms in active and reactive power dynamics, yet the stability of the system is analyzed based on the linearized small-signal model.

To allow a wide application of grid-connected VSCs, nonlinear control and stability analysis approaches are needed, e.g., the Lyapunov method [22]. In [23], a Lyapunov-based controller is developed for a generalized grid-connected VSC to regulate its power outputs. Further, Altin *et. al.* [5] designed a sliding-mode controller in the natural frame with a reduced number of voltage and current sensors. However, these algorithms require accurate information of the system, e.g., transmission line parameters, grid frequency and voltage, etc., which is difficult to obtain in practice. To relax this requirement, a robust DPC is designed where the parameter uncertainties are compensated by a robust design [24]. But

Manuscript received November 4, 2020; revised February 15, 2021; accepted February 25, 2021. This work was supported in part by the Aalborg University Talent Management Program, and in part by the Marie Skłodowska-Curie Actions Individual Fellowships (H2020-MSCA-IF-2020) under Grant 101031512 (FRESLING). *(Corresponding author: Xiongfei Wang.)*

The authors are with the Department of Energy Technology, Aalborg University, 9220 Aalborg, Denmark (e-mail: bof@et.aau.dk; xwa@et.aau.dk).

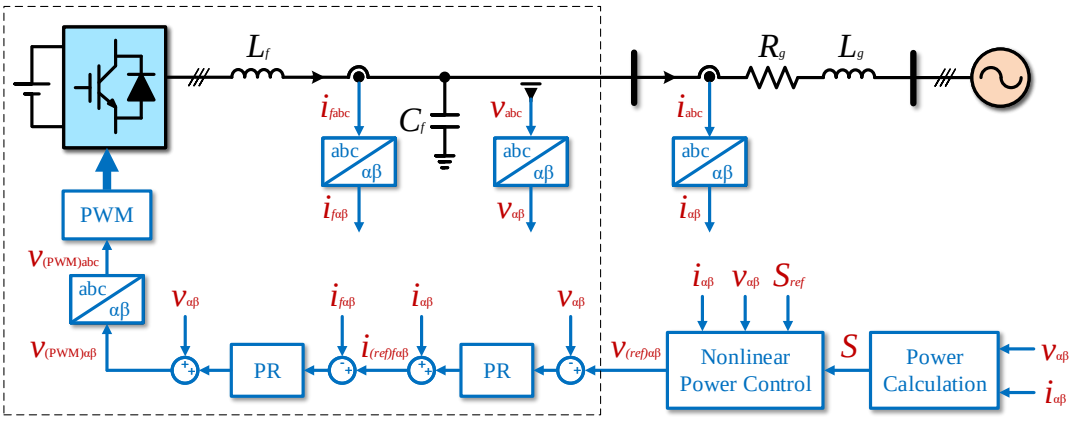

Fig. 1. Overall control diagram of a grid-connected VSC.

the discontinuous signum function used in the robust design can introduce high-frequency oscillations in the voltage control signals, which increases the power losses of power converters. Moreover, the upper bounds of parameter uncertainties are still required in the robust DPC. Therefore, there is a need to design a nonlinear power controller for grid-connected VSCs without the requirement of system parameters.

To this end, in this study, a Lyapunov-based nonlinear power control algorithm is proposed to regulate the active and reactive power outputs of grid-connected VSCs. To facilitate the design of control algorithms in the absence of PLLs, the dynamic model of the system is developed in the stationary frame. A virtual resistance is introduced to allow fast power tracking performance and relax the requirement on accurate system parameters. The main contributions of this study are summarized as follows:

1) To meet the control requirement of grid-connected VSCs, a nonlinear power control algorithm is presented in this study to regulate the active and reactive power outputs to track their references accurately;

2) The proposed algorithm can work robustly under a wide range of grid conditions, e.g., temporary grid faults, various short circuit ratios (SCRs). The synchronization of the VSC with the grid can be guaranteed in the presence of grid frequency deviations;

3) The stability and robustness of the closed-loop system are analyzed through the Lyapunov synthesis. The system states are proved to converge to their equilibria exponentially.

The remainder of this article is organized as follows. Section II illustrates the QSL model of a grid-connected VSC along with a virtual resistance. In Section III, the nonlinear control algorithm, as well as its stability and robustness analyses, is developed based on the Lyapunov theory. Experimental results are provided in Section IV to show the merits of the designed algorithm. Finally, Section V concludes this study.

Notation: For a complex variable x, let x^* and $\|x\|$ denote its conjugate and modulus, respectively.

II. Modeling of Grid-Connected VSCs

Fig. 1 illustrates the overall control diagram of a typical three-phase VSC connected to the grid through an LC-filter and a transmission line. Based on the active and reactive power regulation errors, a nonlinear power controller is utilized to adjust the voltage reference of the capacitor to regulate the active and reactive power outputs. The inner dual-loop proportional-resonant (PR) controller is then applied to realize the voltage reference by modulating the PWM signals of the VSC.

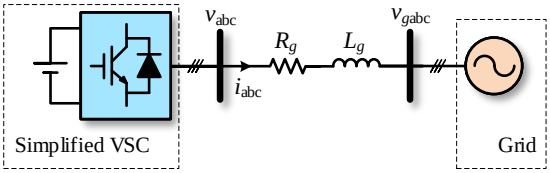

Fig. 2. Simplified topology of a grid-connected VSC.

Since the timescale of the inner dual-loop PR control is designed much faster than that of the outer nonlinear power control, the VSC and its output LC-filter with the inner dual-loop control can be assumed as a voltage source with ideal reference tracking [25], i.e., $v_{\alpha\beta} = v_{(ref)\alpha\beta}$. The simplified topology of the grid-connected VSC is given in Fig. 2.

A. System Model With Virtual Resistance

The dynamics of the simplified system given in Fig. 2 can be expressed as

$$\begin{cases} L_g \dot{i}_{\rm a} + R_g i_{\rm a} = v_{\rm a} - v_{g\rm a} \\ L_g \dot{i}_{\rm b} + R_g i_{\rm b} = v_{\rm b} - v_{g\rm b} \\ L_g \dot{i}_{\rm c} + R_g i_{\rm c} = v_{\rm c} - v_{g\rm c} \end{cases} \tag{1}$$

where $L_g > 0$, $R_g > 0$ are the unknown inductance and resistance of the transmission line, $i_{\rm a}$, $i_{\rm b}$, $i_{\rm c}$ denote the output currents, $v_{g\rm a}$, $v_{g\rm b}$, $v_{g\rm c}$ denote the grid voltages, and $v_{\rm a}$, $v_{\rm b}$, $v_{\rm c}$ denote the output voltages which are treated as the control inputs of the simplified system. Next, according to the Clark transformation, the line dynamic model in the stationary frame (α-β frame) is given as

$$\begin{cases} L_g \dot{i}_{\alpha} + R_g i_{\alpha} = v_{\alpha} - v_{g\alpha} \\ L_g \dot{i}_{\beta} + R_g i_{\beta} = v_{\beta} - v_{g\beta} \end{cases} \tag{2}$$

where i_α, i_β denote the transformed output currents, $v_{g\alpha}$, $v_{g\beta}$ denote the transformed grid voltages, and v_α, v_β denote the transformed voltage control inputs.

Based on the linear system theory [26], for given voltage control inputs v_α and v_β, it can be proved that the line currents i_α, i_β will exponentially converge to their steady-state trajectories with a convergence rate of R_g/L_g. Therefore, to allow fast power tracking performance, it requires that the output currents converge to their steady-state trajectories fast enough. Hence, a virtual resistance is applied in this study to obtain a larger output current convergence rate, which is expressed

$$\begin{cases} v_\alpha = u_\alpha - R_v i_\alpha \\ v_\beta = u_\beta - R_v i_\beta \end{cases} \tag{3}$$

where R_v denotes the virtual resistance, u_α and u_β denotes the virtual voltage control inputs behind the virtual resistance. Substituting (3) into (2) yields the system dynamics with the virtual resistance as

$$\begin{cases} L_g \dot{i}_\alpha + (R_g + R_v) i_\alpha = u_\alpha - v_{g\alpha} \\ L_g \dot{i}_\beta + (R_g + R_v) i_\beta = u_\beta - v_{g\beta} \end{cases}. \tag{4}$$

Hence, for given virtual voltage control inputs u_α, u_β, the line currents i_α, i_β will exponentially converge to their steady-state trajectories with a convergence rate of $(R_g + R_v)/L_g$, which is larger than the original one R_g/L_g with a positive virtual resistance R_v. Moreover, a larger R_v allows the designs of power controllers with faster power tracking performance.

Thereafter, as in [27], [28], the QSL approximation is applied for system (2) to allow simple control designs. In the α-β frame, the QSL impedance model of (4) can be expressed as

$$\begin{cases} -\omega_g L_g i_\beta + (R_g + R_v) i_\alpha = u_\alpha - v_{g\alpha} \\ \omega_g L_g i_\alpha + (R_g + R_v) i_\beta = u_\beta - v_{g\beta} \end{cases}. \tag{5}$$

where ω_g is the angular frequency of the grid voltage $v_{g\text{abc}}$.

For ease of expression, define $v_{\alpha\beta} = v_\alpha + \mathrm{j}v_\beta$, $u_{\alpha\beta} = u_\alpha + \mathrm{j}u_\beta$, $v_{g\alpha\beta} = v_{g\alpha} + \mathrm{j}v_{g\beta}$, and $i_{\alpha\beta} = i_\alpha + \mathrm{j}i_\beta$ with j being the imaginary unit. The relationship between $v_{\alpha\beta}$ and $u_{\alpha\beta}$ can be then expressed as

$$v_{\alpha\beta} = u_{\alpha\beta} - R_v i_{\alpha\beta} \tag{6}$$

and the system model (5) can be rewritten as

$$i_{\alpha\beta} = Y_v u_{\alpha\beta} - Y_v v_{g\alpha\beta} \tag{7}$$

where $Y_v = 1/(R_g + R_v + \mathrm{j}\omega_g L_g)$ represents the virtual line admittance.

B. Control Objective

The instantaneous active and reactive power outputs (P and Q) of the VSC can be expressed as

$$\begin{cases} P = \frac{3}{2}(v_\alpha i_\alpha + v_\beta i_\beta) \\ Q = \frac{3}{2}(v_\beta i_\alpha - v_\alpha i_\beta) \end{cases}. \tag{8}$$

In this study, the main control objective is to regulate the active and reactive power outputs of the VSC to track given references (P_{ref} and Q_{ref}). Based on (8), the complex power regulation error is defined as

$$e_S = S - S_{ref} = \frac{3}{2} v_{\alpha\beta} i^*_{\alpha\beta} - S_{ref} \tag{9}$$

where $S = P + \mathrm{j}Q$ denotes the complex apparent power output, $S_{ref} = P_{ref} + \mathrm{j}Q_{ref}$ denotes the complex apparent power reference. Hence, the control objective is achieved if $e_S = 0$ holds in the steady-state.

III. Control Methodology

A. Lyapunov-Based Control Design and Stability Analysis

In this section, a nonlinear power controller based on the Lyapunov theory is presented to achieve the control objective defined in Section II-B.

According to the Lyapunov theory, for a function W that is positive definite with respect to e_S, if $\dot{W} \le -\lambda W$ with λ being a positive constant, then e_S is bounded for all time and will converge to zero exponentially. Based on this principle, consider the Lyapunov function candidate $W = \|e_S\|^2$, whose time derivative is

$$\dot{W} = e^*_S \dot{e}_S + e_S \dot{e}^*_S. \tag{10}$$

The time derivative of e_S can be given as

$$\begin{aligned} \dot{e}_S =& \frac{3}{2}(1 - R_v Y_v) i^*_{\alpha\beta} (\dot{u}_{\alpha\beta} - \mathrm{j}\omega_g u_{\alpha\beta}) \\ &+ \frac{3}{2} Y^*_v v_{\alpha\beta} (\dot{u}^*_{\alpha\beta} + \mathrm{j}\omega_g u^*_{\alpha\beta}). \end{aligned} \tag{11}$$

The detailed mathematical deduction procedure for $\dot{e}_S$ can be found in Appendix A.

Next, based on $\dot{W}$ and the power regulation error dynamics in (11), a nonlinear power control law is designed as

$$\dot{u}_{\alpha\beta} = -k v_{\alpha\beta} e^*_S + \mathrm{j}\omega_g u_{\alpha\beta} \tag{12}$$

where $k = k_R + \mathrm{j}k_X$ is a user-defined control gain with k_R and k_X being two non-negative constants whose selections will be discussed later. Notice that the first part in (12) is designed to generate a negative definite term in $\dot{W}$. The second part is to compensate the dynamic term $\mathrm{j}\omega_g u_{\alpha\beta}$ in (11).

Now, substituting (12) into the time derivative of e_S yields the closed-loop system dynamics as

$$\dot{e}_S = -(1 - R_v Y_v) k S e^*_S - \frac{3}{2} k^* Y^*_v \|v_{\alpha\beta}\|^2 e_S. \tag{13}$$

Then $\dot{W}$ becomes

$$\begin{aligned} \dot{W} =& -(1 - R_v Y_v) k S e^{*2}_S - \frac{3}{2} k^* Y^*_v \|v_{\alpha\beta}\|^2 \|e_S\|^2 \\ &- (1 - R_v Y^*_v) k^* S^* e^2_S - \frac{3}{2} k Y_v \|v_{\alpha\beta}\|^2 \|e_S\|^2. \end{aligned} \tag{14}$$

Therefore, the stability of the closed-loop system can be guaranteed if $\dot{W}$ is negative definite. By exploring the conditions for $\dot{W} \le 0$, the stability results of the proposed controller (12) are stated in the following theorem.

Theorem 1: Considering a grid-connected VSC modeled by (7), if the power controller is designed as (12), then e_S will converge to zero exponentially if

$$\left\| 1 - \frac{v_{g\alpha\beta}}{v_{\alpha\beta}} \right\| < K \tag{15}$$

where K is a constant dependent on the control parameter k and the virtual line admittance Y_v, expressed as

$$K = \frac{k Y_v + k^* Y^*_v}{2\|k\|\|Y_v\|}. \tag{16}$$

Proof: Please see Appendix B. ■

Hence, according to Theorem 1, the complex apparent power output S of the VSC can track its reference S_{ref}

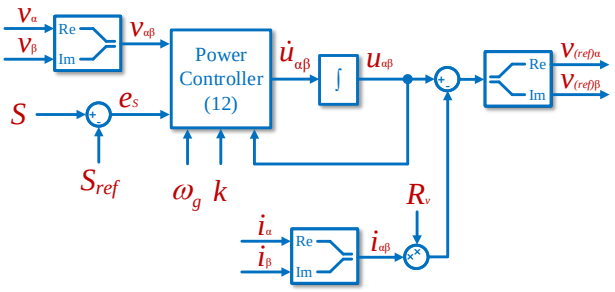

Fig. 3. Diagram of the proposed nonlinear power control algorithm.

accurately with the proposed nonlinear power controller (12) in the steady-state. The control objective is thus achieved.

Moreover, notice that (15) and (16) illustrate the impact of the control parameter k and the virtual line admittance Y_v on the stable operating range of the output voltage $v_{\alpha\beta}$. By recalling the definitions of Y_v and k, the square of (16) can be rewritten as

$$K^2 = \frac{(k_R(R_g + R_v) + k_X\omega_g L_g)^2}{(k_R^2 + k_X^2)((R_g + R_v)^2 + \omega_g^2 L_g^2)}. \tag{17}$$

With the help of the Cauchy-Schwarz inequality, one can obtain that $K \leq 1$ holds, and

$$K = 1 \Leftrightarrow k_X(R_g + R_v) = k_R\omega_g L_g. \tag{18}$$

Hence, the largest stable operating range of the output voltage $v_{\alpha\beta}$ can be obtained if the control gain k is properly selected according to (18).

However, in practice, it is hard to directly select the control parameter k to satisfy (18) due to the the unknown line parameters R_g and L_g. To deal with the line parameter uncertainties, one can select a large enough virtual resistance, e.g., $R_v \geq 2.5/\text{SCR}$ in per unit value. Then the control gain can be simply selected as $k_R > 0$, $k_X = 0$, which is sufficient to ensure an acceptable stable operating range of $v_{\alpha\beta}$ as illustrated in Section IV.

In Fig. 3, the diagram of the proposed nonlinear power control algorithm is demonstrated. With the information of the VSC's active and reactive power outputs and the given power references, the power regulation error e_S is calculated. Further, with the constant ω_g and the user-defined control gain k, the virtual voltage behind the virtual resistance can be obtained by (12). Finally, the output voltage reference can be calculated according to (6) with $v_{\alpha\beta} = v_{(ref)\alpha\beta}$, which is further realized by the inner dual-loop PR controller as shown in Fig. 1.

Remark 1: Notice that based on (6), (7), and $v_{\alpha\beta} = V\exp(\mathrm{j}\theta)$, the controller in (12) can be rewritten as

$$\begin{cases} \dot{\theta} = -\ell_R(Q - Q_{ref}) - \ell_X(P - P_{ref}) + \omega_g \\ \dot{V} = \ell_R V(P - P_{ref}) - \ell_X V(Q - Q_{ref}) \end{cases} \tag{19}$$

where $\ell_R = \mathrm{Re}\{k(1 - R_vY_v)\}$ and $\ell_X = \mathrm{Im}\{k(1 - R_vY_v)\}$ are two constants. Hence, the proposed nonlinear power control algorithm becomes an integral controller of the coupled power regulation errors with voltage-dependent control gains. However, the integral controller (19) will need a longer time to adjust e_S to zero compared to the proposed method since it eliminates the positive impact of R_v on the convergence speed of the line current. Besides, when the grid angular frequency ω_g is not equal to the nominal one, the proposed controller cannot be simply expressed as an integral one given in (19).

Remark 2: It should be noted that for VSCs with L-filters, the dual-loop PR controller is not required. The voltage reference $v_{(ref)\alpha\beta}$ will be directly used for the modulation of the VSC. The proposed control algorithm becomes a DPC one [18].

B. Robustness Analysis

As illustrated in (15), the stable operating range of the proposed power controller is given. Hence, the proposed controller is robust against grid contingencies if (15) is not violated, and thus allows a wide range of grid conditions, such as temporary grid voltage drops, various SCRs, etc. Besides, the accurate power tracking performance can still be achieved in the steady-state if the equilibrium points exist.

Notice that the theoretical results obtained in Theorem 1 is based on the condition that the angular frequency in (12) is exactly the one of the grid. However, in practice, the grid angular frequency may deviate from its nominal value and the proposed power controller should be able to synchronize with the grid in the presence of PLLs.

For ease of exposition, (12) is rewritten as

$$\dot{u}_{\alpha\beta} = -kv_{\alpha\beta}e_S^* + \mathrm{j}\omega_{g0}u_{\alpha\beta} \tag{20}$$

with the constant ω_{g0} being the nominal grid angular frequency, which can be further expressed as

$$\dot{u}_{\alpha\beta} = -kv_{\alpha\beta}e_S^* - \mathrm{j}\tilde{\omega}_g u_{\alpha\beta} + \mathrm{j}\omega_g u_{\alpha\beta} = -kv_{\alpha\beta}z^* + \mathrm{j}\omega_g u_{\alpha\beta} \tag{21}$$

where $\tilde{\omega}_g = \omega_g - \omega_{g0}$ is the error between the grid angular frequency and its nominal one, and

$$z = e_S - \frac{\mathrm{j}\tilde{\omega}_g}{k^*}\frac{u_{\alpha\beta}^*}{v_{\alpha\beta}^*}. \tag{22}$$

Notice that according to (21), the VSC can synchronize with the grid if $z = 0$ in the steady-state.

Based on the Lyapunov theory, the following theorem can be given regarding the control law (20).

Theorem 2: Considering a grid-connected VSC modeled by (7), if the power controller is designed as (20), then z will converge to zero exponentially if

$$\left\| 1 - \frac{v_{g\alpha\beta}}{v_{\alpha\beta}} \right\| < K - \frac{16|\tilde{\omega}_g|R_v}{3\|k\|\|v_{g\alpha\beta}\|^2}. \tag{23}$$

The VSC can maintain synchronization with the grid in the steady-state.

Proof: Please see Appendix C. ■

Therefore, compared with (15), one can notice that the stable operating region of $v_{\alpha\beta}$ in (23) is reduced due to the deviation between ω_{g0} and ω_g. According to Theorem 2, z will converge to zero exponentially instead of e_S. Similar to the idea of the power synchronization control (PSC) [29], according to (22), the power regulation error e_S will converge gradually to frequency deviations between the VSC and the grid to keep the VSC synchronized with the grid. Thus, the

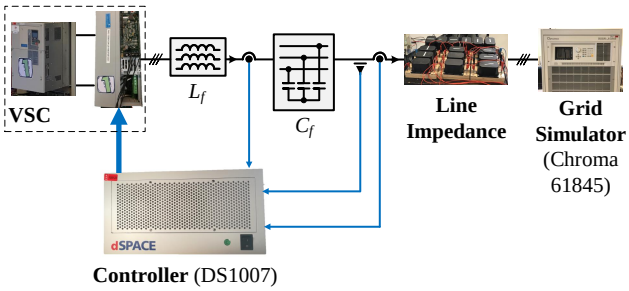

Fig. 4. Experimental setup.

TABLE I
SYSTEM PARAMETERS

Quantity	Value (Set 1)	Value (Set 2)	Value (Set 3)
Active Power Ref. P_{ref} (kW)	2.0	2.0	2.5
Reactive Power Ref. Q_{ref} (kvar)	0	0	2.0
Line Inductance L_g (mH)	2.0	10.5	17.5
Line ESR R_g (Ω)	≈0.1	≈0.3	≈0.5
Phase to Ground RMS Voltage (V)	110	110	66
Filter Inductance (mH)	1.5		
Filter Capacitance (μF)	15		
Nominal Frequency (Hz)	50		
DC Voltage (V)	700		
Power Filter Bandwidth (Hz)	50		

TABLE II
PARAMETERS OF THE PROPOSED CONTROLLER

Quantity	Value	Quantity	Value
Voltage Loop P Gain	0.1	Voltage Loop R Gain	10
Current Loop P Gain	5	Current Loop R Gain	0
PR Control ω_c	2π	Virtual Resistance R_v	15
Power Control Gain k_R	0.05	Power Control Gain k_X	0

TABLE III
PARAMETERS OF THE PSC-BASED CONTROLLER

Quantity	Value
Active Power Control Gain	0.003
Reactive Power Control P Gain	0.01
Reactive Power Control I Gain	0.3

proposed power control algorithm (20) is robust against grid frequency deviations.

In the case that $\omega_{g0} \neq \omega_g$, one can notice that the accurate power regulation cannot be ensured according to Theorem 2. Fortunately, $\|e_S\|$ can be decreased by increasing $\|k\|$ for better power tracking performance. Moreover, as demonstrated in (23), a larger $\|k\|$ can enlarger the stable operating region of $v_{\alpha\beta}$. The impact of the grid frequency deviations can be alleviated by selecting a proper control gain k, e.g., $k_R \geq 40R_v$ and $k_X = 0$ in per unit value as in Section IV.

Remark 3: In Section II, a precondition used in this study is that the timescale of the inner dual-loop PR control is much faster than that of the nonlinear power control one. If the control gain k_R is too big, then this precondition will not be met and thus the stability of the controller may not be ensured. Hence, k_R must be upper-bounded and cannot be selected openly in practice.

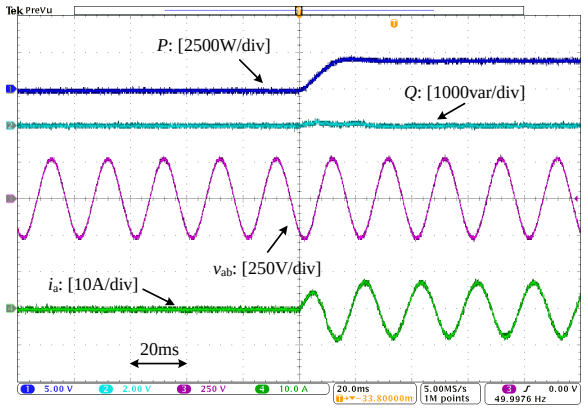

Fig. 5. Control performance of the proposed controller with parameters in Set 1 (SCR≈28.53).

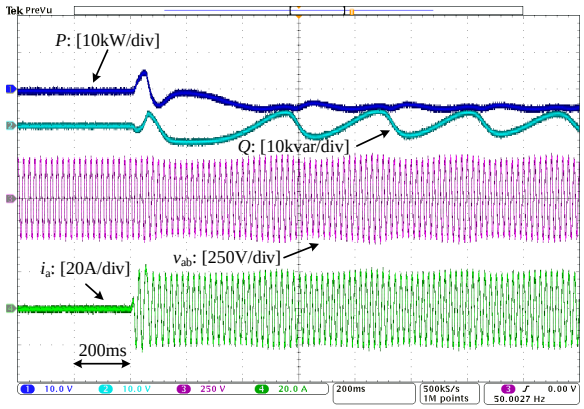

Fig. 6. Control performance of the PSC-based controller with parameters in Set 1 (SCR≈28.53).

IV. VERIFICATION STUDIES

The effectiveness of the proposed nonlinear power control algorithm is tested on a prototype experimental setup as shown in Fig. 4. A three-phase VSC with an LC-filter is connected to a power grid emulated by the Grid Simulator Chroma 61845 through a transmission line. The sampling and switching frequencies are set as 10 kHz. The proposed control algorithm is implemented in the DS1007 PPC processor board with an NXP QorlQ P5020 dual-core real-time processor (64-bit, 2 GHz) and a 32-bit I/O bus. The voltages and currents are measured through the DS2004 high-speed A/D board with a 16-bit resolution and 800 ns conversion time. The switching pulses are generated via the DS5101 digital waveform output board with a 25 ns resolution. The system parameters for different cases are listed in Table I. The control parameters for the dual-loop PR controller and the proposed power controller are given in Table II. To show the advantages of the proposed method, a PSC-based VSC with its reactive power regulated by the PI controller [30] is used for comparison, whose control parameters are shown in Table III.

A. Case I: Power Tracking Performance

Firstly, the system parameters in Set 1 are used. The SCR is approximate 28.53. The corresponding results are illustrated in

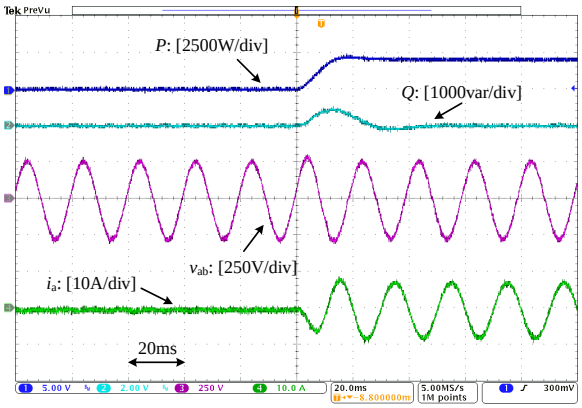

Fig. 7. Control performance of the proposed controller with parameters in Set 2 (SCR≈5.48).

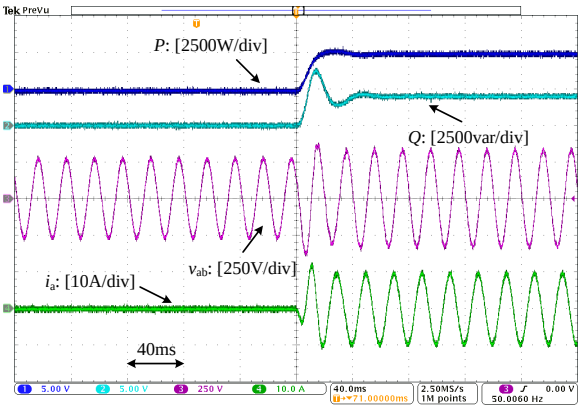

Fig. 9. Control performance of the proposed controller with parameters in Set 3 (SCR≈0.95).

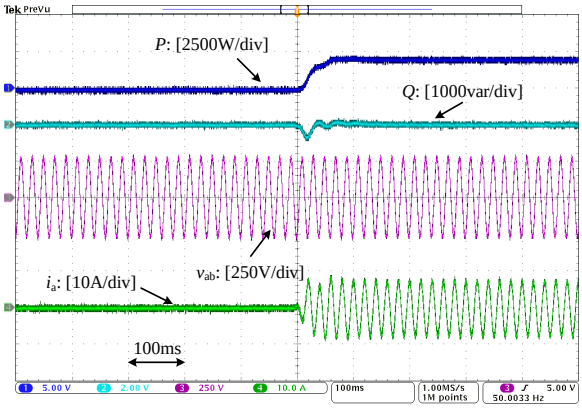

Fig. 8. Control performance of the PSC-based controller with parameters in Set 2 (SCR≈5.48).

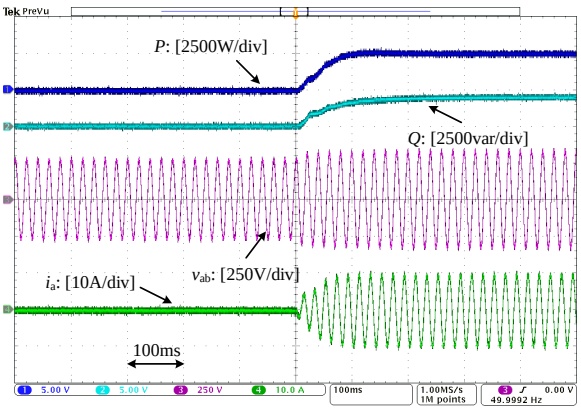

Fig. 10. Control performance of the PSC-based controller with parameters in Set 3 (SCR≈0.95).

Figs. 5-6. From Fig. 5, one can notice that both the active and reactive power outputs can track their references accurately in the steady-state with the proposed method. The settling time is around 20 ms due to the fast regulation of the output voltage and current. However, as shown in Fig. 6, the PSC-based control strategy cannot synchronize the VSC with the grid when the active power reference increases.

Next, the power tracking performance is tested with system parameters in Set 2, where the SCR is approximate 5.5. The experimental results are given in Figs. 7-8. Again, in Fig. 7, one can see that the proposed controller can achieve accurate active and reactive power tracking performance with a settling time of around 30 ms. Besides, from Fig. 8, with the SCR decreases, the PSC-based control strategy can also achieve the active and reactive power tracking objective. However, the settling time is much longer than the proposed method, which is around 100 ms.

Finally, the performance of the proposed and the PSC-based controllers is tested with system parameters in Set 3 with the SCR≈0.95, i.e., the grid is ultra-weak. Notice that in this case, the reactive power reference is selected as 2 kvar to ensure the existence of equilibria. The corresponding results are shown in Figs. 9-10. Again, the power outputs can track their references accurately in the steady-state by both controllers. The settling time of the proposed controller and the PSC-based one is around 50 ms and 200 ms, respectively, which is longer than that of a grid with SCR≈5.5. for both controllers.

B. Case II: Voltage Drop

In this case, the performance of both controllers under the condition that the grid voltage drops from 1 p.u. to 0.6 p.u. for 200 ms is tested. The system parameters in Set 2 are used. The corresponding results are delivered in Figs. 11-12. As shown in Fig. 11, during the grid voltage drop, with the proposed control strategy, the active power output is slightly affected, while the reactive power output deviates from its reference during the transient-state and converges to zero in about 40 ms. The control objective is achieved. In comparison, from Fig. 12, one can see that when the grid voltage drops, the active and reactive power outputs with the PSC-based controller deviate from their set points with the errors around 2500 W and 2500 var, respectively, which are much larger than those of the proposed method.

C. Case III: Frequency Variation

In this case, the control performance when grid frequency decreases 49.7 Hz and increases to 50.3 Hz for 200 ms is tested. Again, the system parameters in Set 2 are used. The corresponding results are shown in Figs. 13-16. From Figs. 13

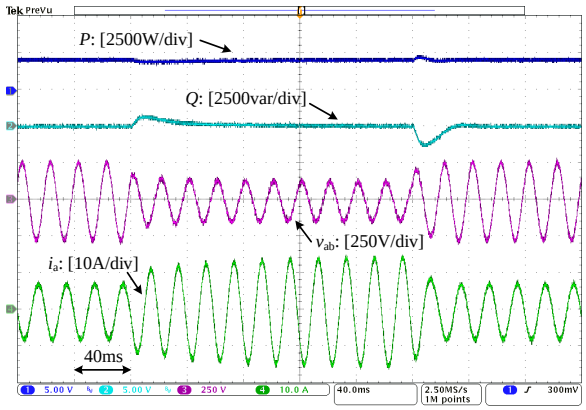

Fig. 11. Control performance of the proposed controller when grid voltage drops to 0.6 p.u.

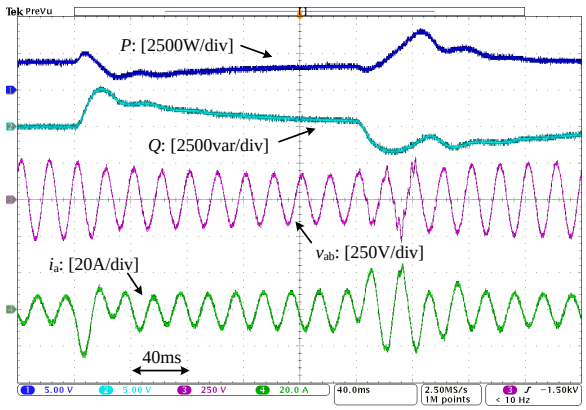

Fig. 12. Control performance of the PSC-based controller when grid voltage drops to 0.6 p.u.

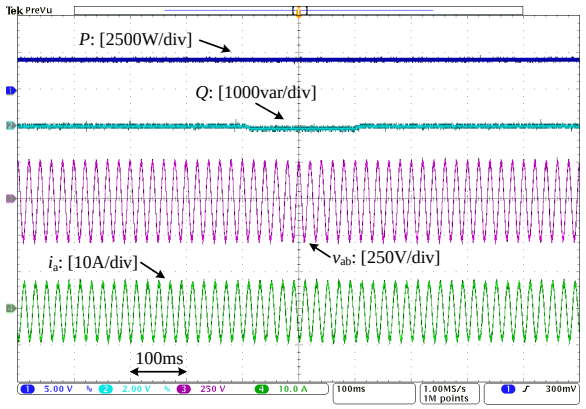

Fig. 13. Control performance of the proposed controller when grid frequency decreases to 49.7 Hz.

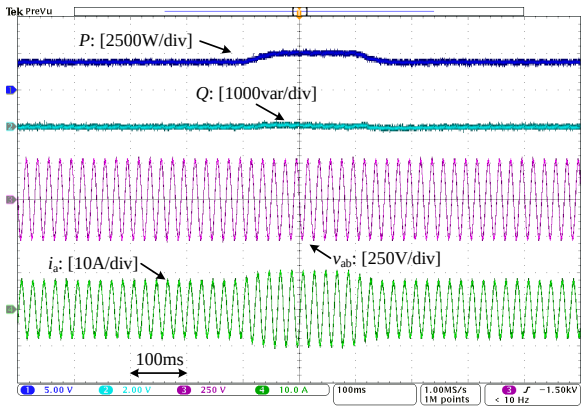

Fig. 14. Control performance of the PSC-based controller when grid frequency decreases to 49.7 Hz.

and 15, one can notice that the active power outputs are almost unaffected, while the reactive power output in the steady-state is no longer zero with a steady-state tracking error around 100 var. According to Theorem 2, when the grid frequency changes, both the active and reactive power outputs cannot accurately track their references if $\tilde{\omega}_g \neq 0$ since the power regulation errors are used to keep the VSC synchronized with the grid. From Figs. 14 and 16, for the PSC-based control methods, the reactive power output is not affected, while the steady-state active power tracking error will be larger than 500 W. Although this steady-state tracking error can be decreased by increasing the active power control gain, the system may suffer from instability issues.

D. Case IV: Voltage Harmonics

In this case, the control performance when a 10% 5th harmonic appears in the grid voltage for 200 ms with the system parameters in Set 2 used. The experimental results are illustrated in Figs. 17-18. One can notice that the active and reactive power tracking performance of both controllers is similar. Compared with the output voltage of the PSC-based controller, which is almost sinusoid, the proposed controller is more sensitive to the harmonics. A possible reason is that the proposed method is more sensitive to the power regulation error to achieve a fast and accurate power tracking performance.

V. Conclusion

In this study, a Lyapunov-based nonlinear control algorithm is presented to achieve the regulation of the active and reactive power outputs of a grid-connected VSC. A virtual resistance is introduced to allow fast power tracking performance and relax the requirement on accurate system parameters. Based on the QSL impedance model, a nonlinear power control algorithm that only utilizes the output voltage and current information is designed. The closed-loop system stability is analyzed via the Lyapunov theory. Theoretical results show that the VSC can keep synchronization with the grid in the presence of grid frequency deviations. Finally, experimental tests under temporary grid faults and various SCRs illustrate the performance and robustness of the proposed control algorithm.

In the future, how to achieve accurate power regulation when grid frequency deviates from its nominal value will be investigated. The explicit relationship between the convergence of the power regulation error and the satisfaction of the requirement on the output voltage will be studied. Besides, the impacts of the inner control loops on the power control performance will be explored.

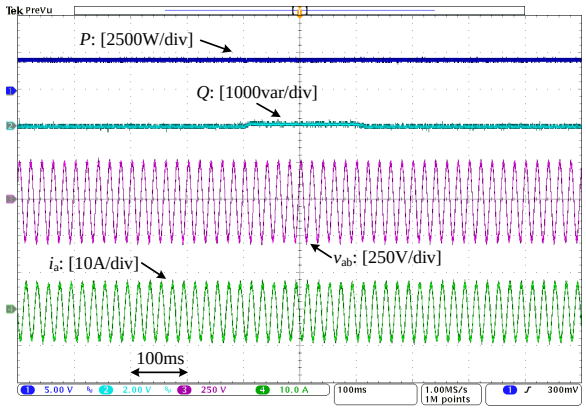

Fig. 15. Control performance of the proposed controller when grid frequency increases to 50.3 Hz.

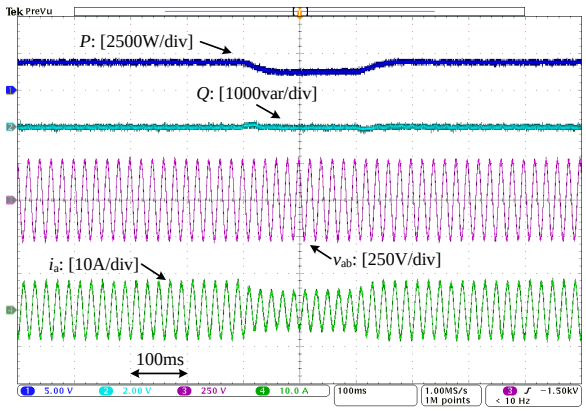

Fig. 16. Control performance of the PSC-based controller when grid frequency increases to 50.3 Hz.

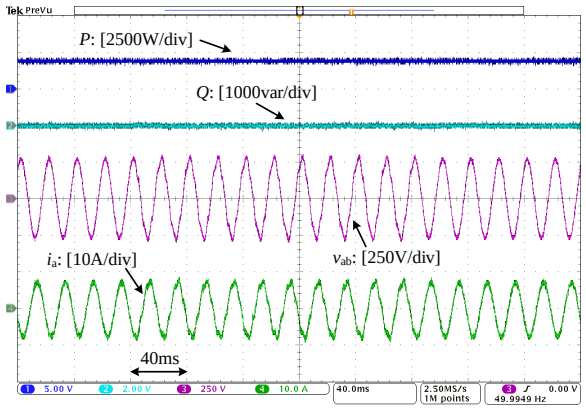

Fig. 17. Control performance of the proposed controller when 10% 5th harmonic appears in grid voltage.

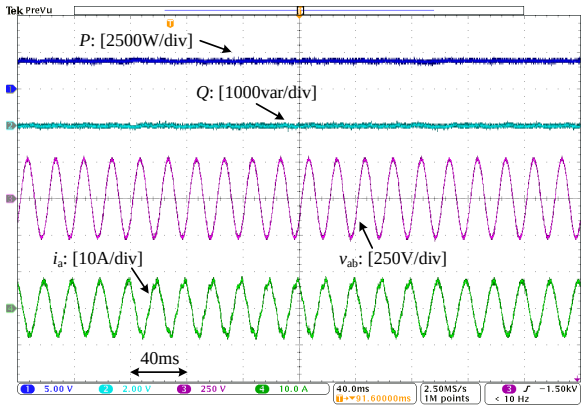

Fig. 18. Control performance of the PSC-based controller when 10% 5th harmonic appears in grid voltage.

APPENDIX A
POWER REGULATION ERROR DYNAMICS

Substituting (6) and (7) into the time derivative of e_S defined in (9) yields

$$\begin{aligned}\dot{e}_S =&\frac{3}{2}i^*_{\alpha\beta}(\dot{u}_{\alpha\beta} - R_v\dot{i}_{\alpha\beta}) + \frac{3}{2}v_{\alpha\beta}\dot{i}^*_{\alpha\beta}\\ =&\frac{3}{2}i^*_{\alpha\beta}\dot{u}_{\alpha\beta} - \frac{3}{2}R_vY_vi^*_{\alpha\beta}(\dot{u}_{\alpha\beta} - \dot{v}_{g\alpha\beta}) + \frac{3}{2}Y^*_v v_{\alpha\beta}(\dot{u}^*_{\alpha\beta} - \dot{v}^*_{g\alpha\beta})\\ =&\frac{3}{2}(1 - R_vY_v)i^*_{\alpha\beta}\dot{u}_{\alpha\beta} + \frac{3}{2}R_vY_vi^*_{\alpha\beta}\dot{v}_{g\alpha\beta} + \frac{3}{2}Y^*_v v_{\alpha\beta}\dot{u}^*_{\alpha\beta}\\ &- \frac{3}{2}Y^*_v v_{\alpha\beta}\dot{v}^*_{g\alpha\beta}.\end{aligned} \tag{24}$$

According to (7), the time derivative of $v_{g\alpha\beta}$ becomes

$$\dot{v}_{g\alpha\beta} = \mathrm{j}\omega_g v_{g\alpha\beta} = \mathrm{j}\omega_g\left(u_{\alpha\beta} - \frac{i_{\alpha\beta}}{Y_v}\right). \tag{25}$$

Then, substituting (25) into (24) yields

$$\begin{aligned}\dot{e}_S =&\frac{3}{2}(1 - R_vY_v)i^*_{\alpha\beta}\dot{u}_{\alpha\beta} + \frac{3}{2}R_vi^*_{\alpha\beta}\mathrm{j}\omega_g(Y_vu_{\alpha\beta} - i_{\alpha\beta})\\ &+ \frac{3}{2}Y^*_v v_{\alpha\beta}\dot{u}^*_{\alpha\beta} + \frac{3}{2}v_{\alpha\beta}\mathrm{j}\omega_g(Y^*_v u^*_{\alpha\beta} - i^*_{\alpha\beta})\\ =&\frac{3}{2}(1 - R_vY_v)i^*_{\alpha\beta}\dot{u}_{\alpha\beta} + \frac{3}{2}Y^*_v v_{\alpha\beta}(\dot{u}^*_{\alpha\beta} + \mathrm{j}\omega_g u^*_{\alpha\beta})\\ &+ \frac{3}{2}R_vY_vi^*_{\alpha\beta}\mathrm{j}\omega_g u_{\alpha\beta} - \frac{3}{2}i^*_{\alpha\beta}\mathrm{j}\omega_g(R_vi_{\alpha\beta} + v_{\alpha\beta}).\end{aligned} \tag{26}$$

Further, by recalling (6), the power regulation error dynamics in (11) can be derived.

APPENDIX B
PROOF OF THEOREM 1

By revoking (15), there exists a constant $0 < \sigma < 1$, such that

$$\left\|1 - \frac{v_{g\alpha\beta}}{v_{\alpha\beta}}\right\| \le \sigma K. \tag{27}$$

According to (6) and (7), the following implication based on (27) can be derived as

$$\begin{aligned}&\left\|1 - \frac{v_{g\alpha\beta}}{v_{\alpha\beta}}\right\| \le \sigma K\\ \Rightarrow&\|kY_v(v_{\alpha\beta} - v_{g\alpha\beta})\|^2 \le \frac{\sigma^2(kY_v + k^*Y^*_v)^2}{4}\|v_{\alpha\beta}\|^2\\ \Rightarrow&\|(1 - R_vY_v)ki_{\alpha\beta}\|^2 \le \frac{\sigma^2(kY_v + k^*Y^*_v)^2}{4}\|v_{\alpha\beta}\|^2\\ \Rightarrow&\|(1 - R_vY_v)kS\|^2 \le \frac{9\sigma^2(kY_v + k^*Y^*_v)^2}{16}\|v_{\alpha\beta}\|^4\\ \Rightarrow&-(1 - R_vY_v)kSe^{*2}_S - (1 - R_vY^*_v)k^*S^*e^2_S\\ &- \frac{3}{2}\sigma(kY_v + k^*Y^*_v)\|v_{\alpha\beta}\|^2\|e_S\|^2 \le 0.\end{aligned} \tag{28}$$

Therefore, $\dot{W}$ in (14) further gives

$$\dot{W} \le -\frac{3}{2}(1-\sigma)(kY_v + k^*Y_v^*)\|v_{\alpha\beta}\|^2\|e_S\|^2. \tag{29}$$

Again, according to (15), the following implication can be derived as

$$\left\|1 - \frac{v_{g\alpha\beta}}{v_{\alpha\beta}}\right\| < K \le 1 \Rightarrow \left\|v_{\alpha\beta} - v_{g\alpha\beta}\right\| < \|v_{\alpha\beta}\|$$
$$\Rightarrow \|v_{\alpha\beta}\| > \frac{\|v_{g\alpha\beta}\|}{2}. \tag{30}$$

Substituting (30) into (29) yields

$$\dot{W} \le -\frac{3}{8}(1-\sigma)(kY_v + k^*Y_v^*)\|v_{g\alpha\beta}\|^2\|e_S\|^2 \le -\lambda W \tag{31}$$

where $\lambda = \frac{3}{8}(1-\sigma)(kY_v + k^*Y_v^*)\|v_{g\alpha\beta}\|^2$. Then,

$$W \le W_0 \exp(-\lambda(t-t_0))$$
$$\Rightarrow \|e_S\| \le \|e_{S0}\| \exp\left(-\frac{\lambda}{2}(t-t_0)\right) \tag{32}$$

where W_0 and e_{S0} are the initial values of W and e_S at time t_0, respectively. Hence, e_S will converge to zero exponentially. The proof is thus completed.

Appendix C
Proof of Theorem 2

Firstly, combining (11) and (21) gives the closed-loop dynamics of the power regulation error as

$$\dot{e}_S = -(1 - R_vY_v)kSz^* - \frac{3}{2}k^*Y_v^*\|v_{\alpha\beta}\|^2 z. \tag{33}$$

To facilitate the stability analysis, substituting (33) into the time derivative of z yields

$$\begin{aligned}\dot{z} =& -(1 - R_vY_v)kSz^* - \frac{3}{2}k^*Y_v^*\|v_{\alpha\beta}\|^2 z \\ & - \frac{\mathrm{j}\tilde{\omega}_g}{k^*}\frac{\dot{u}_{\alpha\beta}^* v_{\alpha\beta}^* - u_{\alpha\beta}^*\dot{v}_{\alpha\beta}^*}{v_{\alpha\beta}^{*2}} \\ =& -(1 - R_vY_v)kSz^* - \frac{3}{2}k^*Y_v^*\|v_{\alpha\beta}\|^2 z \\ & - \frac{\mathrm{j}\tilde{\omega}_g}{k^*}\frac{v_{\alpha\beta}^*(\dot{u}_{\alpha\beta}^* + \mathrm{j}\omega_g u_{\alpha\beta}^*) - u_{\alpha\beta}^*(\dot{v}_{\alpha\beta}^* + \mathrm{j}\omega_g v_{\alpha\beta}^*)}{v_{\alpha\beta}^{*2}}.\end{aligned} \tag{34}$$

Combining (6), (7), and the first equality in (25) yields

$$\dot{v}_{\alpha\beta} - \mathrm{j}\omega_g v_{\alpha\beta} = (1 - R_vY_v)(\dot{u}_{\alpha\beta} - \mathrm{j}\omega_g u_{\alpha\beta}) \tag{35}$$

and

$$v_{\alpha\beta} - (1 - R_vY_v)u_{\alpha\beta} = R_vY_v v_{g\alpha\beta}. \tag{36}$$

Now substituting (35) and (36) into the last term of (34) yields

$$\begin{aligned}\dot{z} =& -(1 - R_vY_v)kSz^* - \frac{3}{2}k^*Y_v^*\|v_{\alpha\beta}\|^2 z \\ & - \frac{\mathrm{j}\tilde{\omega}_g}{k^*}\frac{R_vY_v^* v_{g\alpha\beta}^*(\dot{u}_{\alpha\beta}^* + \mathrm{j}\omega_g u_{\alpha\beta}^*)}{v_{\alpha\beta}^{*2}}.\end{aligned} \tag{37}$$

By invoking the control law in (21), (37) becomes

$$\dot{z} = -(1 - R_vY_v)kSz^* - \frac{3}{2}k^*Y_v^*\|v_{\alpha\beta}\|^2 z - \mathrm{j}\tilde{\omega}_g R_vY_v^*\frac{v_{g\alpha\beta}^*}{v_{\alpha\beta}^*}z. \tag{38}$$

Again, consider the Lyapunov function candidate $W = \|z\|^2$, whose derivative with respect to time is

$$\begin{aligned}\dot{W} =& z^*\dot{z} + z\dot{z}^* \\ =& -(1 - R_vY_v)kSz^{*2} - \frac{3}{2}k^*Y_v^*\|v_{\alpha\beta}\|^2\|z\|^2 \\ & - (1 - R_vY_v^*)k^*S^*z^2 - \frac{3}{2}kY_v\|v_{\alpha\beta}\|^2\|z\|^2 \\ & - \mathrm{j}\tilde{\omega}_g R_vY_v^*\frac{v_{g\alpha\beta}^*}{v_{\alpha\beta}^*}\|z\|^2 + \mathrm{j}\tilde{\omega}_g R_vY_v\frac{v_{g\alpha\beta}}{v_{\alpha\beta}}\|z\|^2.\end{aligned} \tag{39}$$

With the help of (30), (23) becomes

$$\left\|1 - \frac{v_{g\alpha\beta}}{v_{\alpha\beta}}\right\| < K - \frac{2|\tilde{\omega}_g|R_v\|v_{g\alpha\beta}\|}{3\|k\|\|v_{\alpha\beta}\|^3}. \tag{40}$$

Subsequently, there exist two constants $0 \le \epsilon < 1$, $0 < \sigma < 1$ satisfying

$$\left\|1 - \frac{v_{g\alpha\beta}}{v_{\alpha\beta}}\right\| \le \sigma(1-\epsilon)K \tag{41}$$

and

$$|\tilde{\omega}_g|R_v\frac{\|v_{g\alpha\beta}\|}{\|v_{\alpha\beta}\|^3} \le \frac{3}{2}\|k\|\epsilon K. \tag{42}$$

Similar to (28), (41) gives

$$\begin{aligned}& -(1 - R_vY_v)kSz^{*2} - (1 - R_vY_v^*)k^*S^*z^2 \\ & - \frac{3}{2}\sigma(1-\epsilon)(kY_v + k^*Y_v^*)\|v_{\alpha\beta}\|^2\|z\|^2 \le 0.\end{aligned} \tag{43}$$

Hence, $\dot{W}$ becomes

$$\begin{aligned}\dot{W} \le& -\frac{3}{2}(1-\sigma)(1-\epsilon)(kY_v + k^*Y_v^*)\|v_{\alpha\beta}\|^2\|z\|^2 \\ & - \frac{3}{2}\epsilon(kY_v + k^*Y_v^*)\|v_{\alpha\beta}\|^2\|z\|^2 - \mathrm{j}\tilde{\omega}_g R_vY_v^*\frac{v_{g\alpha\beta}^*}{v_{\alpha\beta}^*}\|z\|^2 \\ & + \mathrm{j}\tilde{\omega}_g R_vY_v\frac{v_{g\alpha\beta}}{v_{\alpha\beta}}\|z\|^2.\end{aligned} \tag{44}$$

With the help of the Cauchy-Schwarz inequality and (42), the last two terms in (44) satisfy

$$\begin{aligned}& -\mathrm{j}\tilde{\omega}_g R_vY_v^*\frac{v_{g\alpha\beta}^*}{v_{\alpha\beta}^*}\|z\|^2 + \mathrm{j}\tilde{\omega}_g R_vY_v\frac{v_{g\alpha\beta}}{v_{\alpha\beta}}\|z\|^2 \\ & \le |\tilde{\omega}_g|\left|\mathrm{j}R_v\left(Y_v\frac{v_{g\alpha\beta}}{v_{\alpha\beta}} - Y_v^*\frac{v_{g\alpha\beta}^*}{v_{\alpha\beta}^*}\right)\right|\|z\|^2 \\ & \le 2|\tilde{\omega}_g|R_v\|Y_v\|\left\|\frac{v_{g\alpha\beta}}{v_{\alpha\beta}}\right\|\|z\|^2 \\ & \le 3\epsilon\|k\|\|Y_v\|K\|v_{\alpha\beta}\|^2\|z\|^2 \\ & = \frac{3}{2}\epsilon(kY_v + k^*Y_v^*)\|v_{\alpha\beta}\|^2\|z\|^2.\end{aligned} \tag{45}$$

Afterward, (44) can be simplified as

$$\dot{W} \le -\frac{3}{2}(1-\sigma)(1-\epsilon)(kY_v + k^*Y_v^*)\|v_{\alpha\beta}\|^2\|z\|^2. \tag{46}$$

Substituting (30) into (46) yields

$$\dot{W} \le -\frac{3}{8}(1-\sigma)(1-\epsilon)(kY_v + k^*Y_v^*)\|v_{g\alpha\beta}\|^2\|z\|^2 \le -\lambda W \tag{47}$$

where $\lambda = \frac{3}{8}(1-\sigma)(1-\epsilon)(kY_v + k^*Y_v^*)\|v_{g\alpha\beta}\|^2$. Next,

$$W \le W_0 \exp(-\lambda(t-t_0))$$
$$\Rightarrow \|z\| \le \|z_0\| \exp\left(-\frac{\lambda}{2}(t-t_0)\right) \quad (48)$$

with W_0 and z_0 being the initial values of W and z at time t_0, respectively. Therefore, z will converge to zero asymptotically. Furthermore, combining (21) and (35) gives

$$\lim_{t\to\infty} z = 0 \Rightarrow \lim_{t\to\infty} \dot{u}_{\alpha\beta} = \mathrm{j}\omega_g u_{\alpha\beta} \Rightarrow \lim_{t\to\infty} \dot{v}_{\alpha\beta} = \mathrm{j}\omega_g v_{\alpha\beta} \quad (49)$$

which means that both $u_{\alpha\beta}$ and $v_{\alpha\beta}$ are variables with an angular frequency of ω_g in the steady-state. Hence, the VSC can synchronize with the grid automatically. The proof is thus completed.

REFERENCES

[1] B. Fan, J. Peng, J. Duan, Q. Yang, and W. Liu, "Distributed control of multiple-bus microgrid with paralleled distributed generators," *IEEE/CAA J. Automatica Sinica*, vol. 6, no. 3, pp. 676–684, 2019.

[2] K. Koiwa, K.-Z. Liu, T. Zanma, Y. Li, and J. Tamura, "Full converter control for variable speed wind turbines without integral controller or PLL," *IEEE Trans. Ind. Electron.*, to be published, doi: 10.1109/TIE.2019.2955406.

[3] N. G. Hingorani, "Flexible AC transmission," *IEEE Spectr.*, vol. 30, no. 4, pp. 40–45, 1993.

[4] L. Guo, N. Jin, Y. Li, and K. Luo, "A model predictive control method for grid-connected power converters without AC voltage sensors," *IEEE Trans. Ind. Electron.*, to be published, doi: 10.1109/TIE.2020.2970638.

[5] N. Altin, S. Ozdemir, H. Komurcugil, and I. Sefa, "Sliding-mode control in natural frame with reduced number of sensors for three-phase grid-tied LCL-interfaced inverters," *IEEE Trans. Ind. Electron.*, vol. 66, no. 4, pp. 2903–2913, 2019.

[6] R. Ottersten and J. Svensson, "Vector current controlled voltage source converter-deadbeat control and saturation strategies," *IEEE Trans. Power Electron.*, vol. 17, no. 2, pp. 279–285, 2002.

[7] R. Kadri, J.-P. Gaubert, and G. Champenois, "An improved maximum power point tracking for photovoltaic grid-connected inverter based on voltage-oriented control," *IEEE Trans. Ind. Electron.*, vol. 58, no. 1, pp. 66–75, 2010.

[8] F. Blaabjerg, R. Teodorescu, M. Liserre, and A. V. Timbus, "Overview of control and grid synchronization for distributed power generation systems," *IEEE Trans. Ind. Electron.*, vol. 53, no. 5, pp. 1398–1409, 2006.

[9] D. Dong, B. Wen, D. Boroyevich, P. Mattavelli, and Y. Xue, "Analysis of phase-locked loop low-frequency stability in three-phase grid-connected power converters considering impedance interactions," *IEEE Trans. Ind. Electron.*, vol. 62, no. 1, pp. 310–321, 2014.

[10] L. Harnefors, M. Bongiorno, and S. Lundberg, "Input-admittance calculation and shaping for controlled voltage-source converters," *IEEE Trans. Power Electron.*, vol. 54, no. 6, pp. 3323–3334, 2007.

[11] J. Fang, X. Li, H. Li, and Y. Tang, "Stability improvement for three-phase grid-connected converters through impedance reshaping in quadrature-axis," *IEEE Trans. Power Electron.*, vol. 33, no. 10, pp. 8365–8375, 2018.

[12] D. Zhu, S. Zhou, X. Zou, Y. Kang, and K. Zou, "Small-signal disturbance compensation control for LCL-type grid-connected converter in weak grid," *IEEE Trans. Ind. Appl.*, vol. 56, no. 3, pp. 2852–2861, 2020.

[13] D. Yang, X. Wang, F. Liu, K. Xin, Y. Liu, and F. Blaabjerg, "Symmetrical PLL for SISO impedance modeling and enhanced stability in weak grids," *IEEE Trans. Power Electron.*, vol. 35, no. 2, pp. 1473–1483, 2020.

[14] D. Zhu, S. Zhou, X. Zou, and Y. Kang, "Improved design of PLL controller for LCL-type grid-connected converter in weak grid," *IEEE Trans. Power Electron.*, vol. 35, no. 5, pp. 4715–4727, 2020.

[15] J. Z. Zhou, H. Ding, S. Fan, Y. Zhang, and A. M. Gole, "Impact of short-circuit ratio and phase-locked-loop parameters on the small-signal behavior of a VSC-HVDC converter," *IEEE Trans. Power Del.*, vol. 29, no. 5, pp. 2287–2296, 2014.

[16] H. Wu and X. Wang, "Design-oriented transient stability analysis of PLL-synchronized voltage-source converters," *IEEE Trans. Power Electron.*, vol. 35, no. 4, pp. 3573–3589, 2020.

[17] Q. Hu, L. Fu, F. Ma, and F. Ji, "Large signal synchronizing instability of PLL-based VSC connected to weak AC grid," *IEEE Trans. Power Syst.*, vol. 34, no. 4, pp. 3220–3229, 2020.

[18] T. Noguchi, H. Tomiki, S. Kondo, and I. Takahashi, "Direct power control of PWM converter without power-source voltage sensors," *IEEE Trans. Ind. Appl.*, vol. 34, no. 3, pp. 473–479, 1998.

[19] J. Scoltock, T. Geyer, and U. K. Madawala, "Model predictive direct power control for grid-connected NPC converters," *IEEE Trans. Ind. Electron.*, vol. 62, no. 9, pp. 5319–5328, 2015.

[20] M. Malinowski, M. Jasinski, and M. P. Kazmierkowski, "Simple direct power control of three-phase PWM rectifier using space-vector modulation (DPC-SVM)," *IEEE Trans. Ind. Electron.*, vol. 51, no. 2, pp. 447–454, 2004.

[21] Y. Gui, X. Wang, H. Wu, and F. Blaabjerg, "Voltage-modulated direct power control for a weak grid-connected voltage source inverters," *IEEE Trans. Power Electron.*, vol. 34, no. 11, pp. 11 383–11 395, 2019.

[22] H. Komurcugil and O. Kukrer, "Lyapunov-based control for three-phase PWM AC/DC voltage-source converters," *IEEE Trans. Power Electron.*, vol. 13, no. 5, pp. 801–813, 1998.

[23] S. Dasgupta, S. N. Mohan, S. K. Sahoo, and S. K. Panda, "Lyapunov function-based current controller to control active and reactive power flow from a renewable energy source to a generalized three-phase microgrid system," *IEEE Trans. Ind. Electron.*, vol. 60, no. 2, pp. 799–813, 2013.

[24] Y. Gui, C. Kim, C. C. Chung, J. M. Guerrero, Y. Guan, and J. C. Vasquez, "Improved direct power control for grid-connected voltage source converters," *IEEE Trans. Ind. Electron.*, vol. 65, no. 10, pp. 8041–8051, 2018.

[25] D. Pan, X. Wang, F. Liu, and R. Shi, "Transient stability of voltage-source converters with grid-forming control: A design-oriented study," *IEEE J. Emerg. Sel. Topics Power Electron.*, vol. 8, no. 2, pp. 1019–1033, 2020.

[26] C.-T. Chen, *Linear system theory and design*, 3rd ed. New York, NY, USA: Oxford University Press, 1999.

[27] V. Venkatasubramanian, H. Schattler, and J. Zaborszky, "Fast time-varying phasor analysis in the balanced three-phase large electric power system," *IEEE Trans. Autom. Control*, vol. 40, no. 11, pp. 1975–1982, 1995.

[28] S. Riverso, F. Sarzo, and G. Ferrari-Trecate, "Plug-and-play voltage and frequency control of islanded microgrids with meshed topology," *IEEE Trans. Smart Grid*, vol. 6, no. 3, pp. 1176–1184, 2015.

[29] L. Zhang, L. Harnefors, and H.-P. Nee, "Power-synchronization control of grid-connected voltage-source converters," *IEEE Trans. Power Syst.*, vol. 25, no. 2, pp. 809–820, 2009.

[30] S. Yazdani, M. Ferdowsi, M. Davari, and P. Shamsi, "Advanced current-limiting and power-sharing control in a PV-based grid-forming inverter under unbalanced grid conditions," *IEEE J. Emerg. Sel. Topics Power Electron.*, vol. 8, no. 2, pp. 1084–1096, 2020.

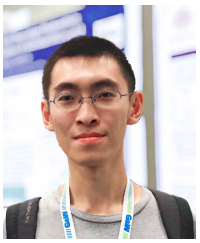

Bo Fan (S'15-M'20) received the B.S. degree in automation and the Ph.D. degree in control science and engineering from Zhejiang University, Hangzhou, China, in 2014 and 2019, respectively.

Since 2020, he has been with the Department of Energy Technology, Aalborg University, Aalborg, Denmark, where he is currently a Postdoctoral Researcher. His research interests include distributed control, nonlinear systems, smart grid, and renewable energy systems.

Dr. Fan was the recipient of the 2019 Outstanding Reviewer Award of IEEE TRANSACTIONS ON POWER SYSTEMS and the 2019 Best Reviewer Award of IEEE TRANSACTIONS ON SMART GRID.

Xiongfei Wang (S'10-M'13-SM'17) received the B.S. degree from Yanshan University, Qinhuangdao, China, in 2006, the M.S. degree from Harbin Institute of Technology, Harbin, China, in 2008, both in electrical engineering, and the Ph.D. degree in energy technology from Aalborg University, Aalborg, Denmark, in 2013.

Since 2009, he has been with the Department of Energy Technology, Aalborg University, Aalborg, Denmark, where he became an Assistant Professor in 2014, an Associate Professor in 2016, a Professor and Research Program Leader for Electronic Power Grid (eGrid) in 2018. He is also a Visiting Professor of KTH Royal Institute of Technology, Stockholm, Sweden, from 2020. His research interests include modeling, dynamic analysis and control of power electronic converters and systems, power electronics for sustainable energy systems and electrical grids, high power converters and multi-converter systems.

Dr. Wang was selected into Aalborg University Strategic Talent Management Program in 2016. He was the recipient of six IEEE Prize Paper Awards, the 2016 Outstanding Reviewer Award of IEEE TRANSACTIONS ON POWER ELECTRONICS, the 2018 IEEE PELS Richard M. Bass Outstanding Young Power Electronics Engineer Award, the 2019 IEEE PELS Sustainable Energy Systems Technical Achievement Award, the 2020 IEEE Power & Energy Society Prize Paper Award, and the Highly Cited Researcher in the Web of Science in 2019-2020. He serves as a Member-at-Large of Administrative Committee for the IEEE Power Electronics Society in 2020-2022, a Co-Editor-in-Chief for the IEEE TRANSACTIONS ON POWER ELECTRONICS, and as an Associate Editor for the IEEE TRANSACTIONS ON INDUSTRY APPLICATIONS and the IEEE JOURNAL OF EMERGING AND SELECTED TOPICS IN POWER ELECTRONICS.